Computer Assisted Mechanics and Engineering Sciences, **17**: 113–135, 2010.
Copyright © 2010 by Institute of Fundamental Technological Research, Polish Academy of Sciences

Mode I crack problems by coupled fractal finite element and meshfree method

B.N. Rao and K.N. Rajesh
Structural Engineering Division
Department of Civil Engineering
Indian Institute of Technology Madras, Chennai 600 036, India
e-mail: bnrao@iitm.ac.in

This paper presents a coupling technique for integrating the fractal finite element method (FFEM) with element-free Galerkin method (EFGM) for analyzing homogeneous, isotropic, and two-dimensional linear-elastic cracked structures subjected to Mode I loading condition. FFEM is adopted for discretization of domain close to the crack tip and EFGM is adopted in the rest of the domain. In the transition region interface elements are employed. The shape functions within interface elements which comprise both the element-free Galerkin and the finite element shape functions, satisfy the consistency condition thus ensuring convergence of the proposed coupled FFEM-EFGM. The proposed method combines the best features of FFEM and EFGM, in the sense that no structured mesh or special enriched basis functions are necessary and no post-processing (employing any path-independent integrals) is needed to determine fracture parameters such as stress-intensity factors (SIFs) and T-stress. The numerical results show that SIFs and T-stress obtained using the proposed method, are in excellent agreement with the reference solutions for the structural and crack geometries considered in the present study. Also a parametric study is carried out to examine the effects of the integration order, the similarity ratio, the number of transformation terms, and the crack-length to width ratio, on the quality of the numerical solutions.

Keywords: crack, Element-free Galerkin method, Fractal Finite Element Method, Stress-Intensity Factor, T-stress, Linear-Elastic Fracture Mechanics, Mode I.

1. Introduction

Recently, the methods based on fractal geometry concepts to generate infinite number of finite elements around the crack tip to capture the crack tip singularity, have been developed or investigated to solve linear-elastic fracture mechanics (LEFM) problems [1–5]. The fractal finite element method (FFEM) is one of such methods developed for calculating SIFs in linear-elastic crack problems. Since its origin, it has been successfully applied to solve many kinds of crack problems under Mode I and mixed mode loading conditions in 2D [6–15] and 3D [16]. Basically, FFEM separates a 2D or 3D cracked elastic body into a regular and a singular regions (see Fig. 1), with the latter enclosing the crack tip. Both the regular and the singular regions are modelled by conventional isoparametric finite elements. However, within the singular region an infinite number of elements are generated by a self-similar, fractal process to capture the singular behaviour at the crack tip. The nodal displacements in the singular region are transformed to a set of unknown coefficients using Williams analytical solution for the displacements near the crack tip [17]. Since the stiffness matrix of an isoparametric element depends only on its shape and not its actual dimensions, the above transformation can be performed at the element level and the results summed up as a geometrical progression series to be assembled to the global stiffness matrix. The contributions of the infinite number of elements in the singular region are therefore fully accounted for, while the number of degrees of freedom involved remains finite.

Compared with other numerical methods like the finite element method (FEM), FFEM has several advantages. First, by using the concept of fractal geometry, infinite number of finite ele-

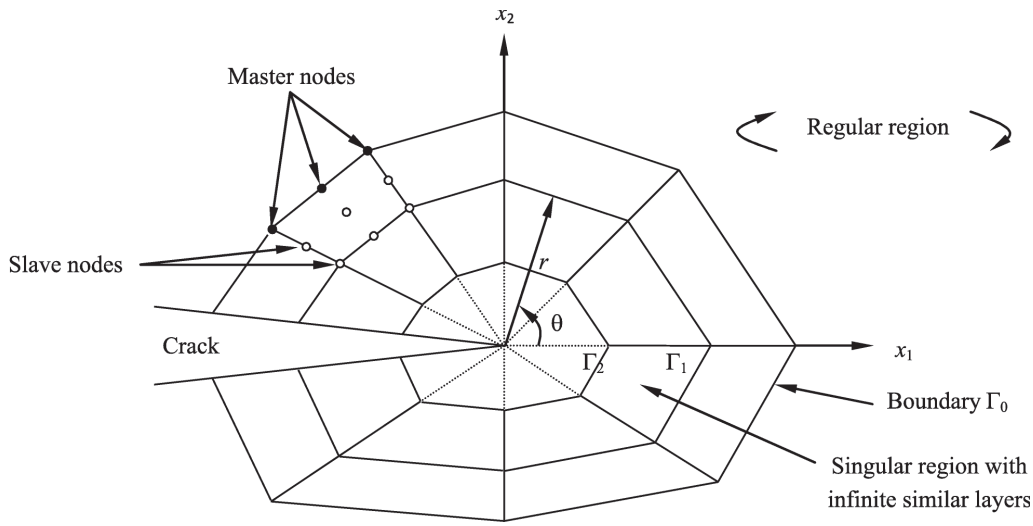

Fig. 1. Cracked body domain with regular region, singular region, and fractal mesh.

ments can be generated virtually around the crack tip, and hence the effort for data preparation is minimized. Second, based on the eigenfunction expansion of the displacement fields [17, 18], the infinite number of finite elements that generate virtually by fractal geometry around the crack tip are transformed in an expeditious manner. This results in reducing the computational time and the memory requirement for fracture analysis of cracked structures. Third, no special finite elements and post–processing are needed to determine the SIFs and T-stress. Finally, as the analytical solution is embodied in the transformation, the accuracy of the predicted SIFs and T-stress is high.

In recent years, as an alternative to FEM, a class of meshfree or meshless methods, such as the element-free Galerkin method (EFGM) [19–21], has emerged to demonstrate significant potential for solving moving boundary problems typified by growing cracks. Fundamental to all meshless methods, a structured mesh is not used, since only a scattered set of nodal points is required in the domain of interest. This feature presents significant implications for modeling fracture propagation, because the domain of interest is completely discretized by a set of nodes. Since no element connectivity data are needed, the burdensome remeshing required by FEM is avoided. A growing crack can be modeled by simply extending the free surfaces, which correspond to the crack. By sidestepping remeshing requirements, crack-propagation analysis can be dramatically simplified.

Although meshless methods are attractive for simulating crack propagation, because of their versatility, the computational cost of a meshless method typically exceeds the cost of a regular FEM. Furthermore, given the level of maturity and comprehensive capabilities of FEM, it is often advantageous to use meshless methods only in the sub-domains, where their capabilities can be exploited to the greatest benefit. In modeling the crack propagation in a complex engineering structure with stiffeners, connections, welds, etc., it is more effective to apply meshless methods at the sites of potential crack growth and FEM in the remainder of the domain. Therefore, numerical methods need to be developed for combining meshless and finite element methods.

This paper presents a coupling technique for integrating FFEM with EFGM for analyzing homogeneous, isotropic, and two-dimensional linear-elastic cracked structures subjected to Mode I loading condition. FFEM is adopted for discretization of domain close to the crack tip and EFGM is adopted in the rest of the domain. In the transition region, interface elements are employed. The interface element shape functions which comprise both the element–free Galerkin and the finite element shape functions, satisfy the consistency condition thus ensuring convergence of the proposed coupled FFEM-EFGM. The proposed method combines the best features of FFEM and EFGM, in the sense that no structured mesh or special enriched basis functions are necessary and no post-processing (employing any path-independent integrals) is needed to determine fracture

parameters such as SIFs and T-stress. Three numerical examples are presented to illustrate the proposed coupled FFEM-EFGM by calculating SIFs and T-stress.

2. Fractal finite element method

As depicted in Fig. 1, FFEM divides the domain of a two-dimensional body into a regular and a singular region, with the latter enclosing the crack tip. In Fig. 1, the boundary curve Γ_0 separates the two regions. Both the regular and singular regions are modeled using conventional finite elements. With the crack tip as the centre of similarity and using ξ as the similarity ratio, an infinite set of curves $\{\Gamma_1, \Gamma_2, \ldots\}$, similar to Γ_0 but with proportional constants $(\xi^1, \xi^2, \ldots)$, are generated inside the singular region. Between the two curves Γ_{k-1} and Γ_k, the region is named the k-th layer. Straight lines that connect the crack tip to the corner nodes lying on Γ_0 are then created, dividing each layer into a mesh of elements with a similar pattern in the process. A fractal mesh is thus generated in the singular region with conventional finite elements only being used. All nodes located on Γ_0 are called the master nodes (m), while those inside Γ_0 are called the slave nodes (s).

2.1. Williams eigenfunction expansion

For a plane crack with traction-free faces subjected to arbitrary far field loading, the linear elastic displacement field at the crack tip obtained by the Williams eigenfunction expansion technique [17] can be expressed as

$$u_1 = \sum_{n=0}^{\infty} \frac{r^{n/2}}{2\mu} \left[a_n \left(\left(\kappa + \frac{n}{2} + (-1)^n \right) \cos \frac{n}{2}\theta - \frac{n}{2} \cos \left(\frac{n}{2} - 2 \right) \theta \right) \right], \tag{1}$$

$$u_2 = \sum_{n=0}^{\infty} \frac{r^{n/2}}{2\mu} \left[a_n \left(\left(\kappa - \frac{n}{2} - (-1)^n \right) \sin \frac{n}{2}\theta + \frac{n}{2} \sin \left(\frac{n}{2} - 2 \right) \theta \right) \right], \tag{2}$$

where μ is the shear modulus, (r, θ) are the polar coordinates, $\kappa = (3-\nu)/(1+\nu)$ for plane stress and $\kappa = 3 - 4\nu$ for plane strain, with ν being the Poisson's ratio.

The coefficients a_n can be determined after imposing loading and other boundary conditions. Mode-I SIF, K_I is related to the first degree coefficients (a_1) in the series which is directly associated with the $r^{-1/2}$ term accounting for the singular stress behaviour at the crack tip, as follows:

$$a_1 = \frac{K_I}{\sqrt{2\pi}}. \tag{3}$$

The first non-singular stress term, which acts parallel to the crack tip, of the Williams eigenfunction expansion series and is known as T-stress, can be related to the coefficient (a_2), as follows

$$T = 4a_2. \tag{4}$$

2.2. Fractal transformation

In conventional FEM, according to the conservation of strain energy the stiffness equation system can be written as

$$\mathbf{Kd} = \mathbf{f}, \tag{5}$$

where $\mathbf{K}$ is the stiffness matrix, $\mathbf{d}$ is the nodal displacement vector and $\mathbf{f}$ is the nodal force vector. For the regular region, the stiffness equation system can be partitioned with respect to the nodes other than the master nodes (r) and the master nodes (m) as follows:

$$\begin{bmatrix} \mathbf{K}_{rr}^{R} & \mathbf{K}_{rm}^{R} \\ \mathbf{K}_{mr}^{R} & \mathbf{K}_{mm}^{R} \end{bmatrix} \begin{Bmatrix} \mathbf{d}_r \\ \mathbf{d}_m \end{Bmatrix} = \begin{Bmatrix} \mathbf{f}_r^{R} \\ \mathbf{f}_m^{R} \end{Bmatrix}, \tag{6}$$

where $\mathbf{d}_r$ are the displacements of the nodes in the regular region other than the master nodes (r), and $\mathbf{d}_m$ are the displacements of the master nodes (m), etc. Similarly, for the first layer in the singular region, the stiffness equation system

$$\mathbf{K}^{1st}\mathbf{d}^{1st} = \mathbf{f}^{1st}, \tag{7}$$

can be partitioned with respect to the master nodes (m) and the slave nodes (s) as follows:

$$\begin{bmatrix} \mathbf{K}_{mm}^{1st} & \mathbf{K}_{ms}^{1st} \\ \mathbf{K}_{sm}^{1st} & \mathbf{K}_{ss}^{1st} \end{bmatrix} \begin{Bmatrix} \mathbf{d}_m \\ \mathbf{d}_s^{1st} \end{Bmatrix} = \begin{Bmatrix} \mathbf{f}_m^{1st} \\ \mathbf{f}_s^{1st} \end{Bmatrix}, \tag{8}$$

where $\mathbf{d}_s^{1st}$ are the displacements of the slave nodes (s) in the first layer of the singular region. Using the Williams eigenfunction expansion in Eqs. (1) and (2), $\mathbf{d}_s^{1st}$ can be expressed as a function of the generalized coordinates $\boldsymbol{a} = \{a_0, a_1, a_2, \ldots\}^T$ as

$$\mathbf{d}_s^{1st}(r,\theta) = \mathbf{T}_s^{1st}(r,\theta)\,\boldsymbol{a}, \tag{9}$$

where $\mathbf{T}_s^{1st} = \mathbf{T}_s^{1st}(r,\theta)$ is a transformation matrix in terms of the polar coordinates (r,θ) for the slave nodes (s) in the first layer. Using the transformation matrix $\mathbf{T}_s^{1st}(r,\theta)$ Eq. (8) can be transformed into

$$\begin{bmatrix} \mathbf{K}_{mm}^{1st} & \mathbf{K}_{ms}^{1st}\mathbf{T}_s^{1st} \\ \left(\mathbf{T}_s^{1st}\right)^T \mathbf{K}_{sm}^{1st} & \left(\mathbf{T}_s^{1st}\right)^T \mathbf{K}_{ss}^{1st}\mathbf{T}_s^{1st} \end{bmatrix} \begin{Bmatrix} \mathbf{d}_m \\ \boldsymbol{a} \end{Bmatrix} = \begin{Bmatrix} \mathbf{f}_m^{1st} \\ \left(\mathbf{T}_s^{1st}\right)^T \mathbf{f}_s^{1st} \end{Bmatrix}. \tag{10}$$

Since the second and subsequent layers in the singular region i.e. $k \geq 2$, comprise only the slave nodes (s), the final assembled global stiffness equation system has the form

$$\begin{bmatrix} \mathbf{K}_{rr}^{R} & \mathbf{K}_{rm}^{R} & \mathbf{0} \\ \mathbf{K}_{mr}^{R} & \mathbf{K}_{mm}^{R} + \mathbf{K}_{mm}^{1st} & \overline{\mathbf{K}}_{ms}^{1st} \\ \mathbf{0} & \overline{\mathbf{K}}_{sm}^{1st} & \overline{\mathbf{K}}_{ss}^{1st} + \overline{\mathbf{K}}_{s}^{inn} \end{bmatrix} \begin{Bmatrix} \mathbf{d}_r \\ \mathbf{d}_m \\ \boldsymbol{a} \end{Bmatrix} = \begin{Bmatrix} \mathbf{f}_r^{R} \\ \mathbf{f}_m^{R} + \mathbf{f}_m^{1st} \\ \overline{\mathbf{f}}_s^{1st} + \overline{\mathbf{f}}_s^{inn} \end{Bmatrix}, \tag{11}$$

where $\overline{\mathbf{K}}_{ms}^{1st} = \mathbf{K}_{ms}^{1st}\mathbf{T}_s^{1st}$, $\overline{\mathbf{K}}_{ss}^{1st} = \left(\mathbf{T}_s^{1st}\right)^T \mathbf{K}_{ss}^{1st}\mathbf{T}_s^{1st}$, $\overline{\mathbf{K}}_{s}^{inn} = \sum\limits_{k=2}^{\infty} \left(\mathbf{T}_s^{kth}\right)^T \mathbf{K}_s^{kth}\mathbf{T}_s^{kth}$, $\overline{\mathbf{f}}_s^{1st} = \left(\mathbf{T}_s^{1st}\right)^T \mathbf{f}_s^{1st}$, and $\overline{\mathbf{f}}_s^{inn} = \sum\limits_{k=2}^{\infty} \left(\mathbf{T}_s^{kth}\right)^T \mathbf{f}_s^{kth}$. Finally, $\sum\limits_{k=2}^{\infty} \left(\mathbf{T}_s^{kth}\right)^T \mathbf{K}_s^{kth}\mathbf{T}_s^{kth}$ is a geometrical progression series and so we have

$$\overline{\mathbf{K}}_{s}^{inn} = \left[\xi^{-\frac{n_i+n_j}{2}} - 1\right]^{-1} \left(\mathbf{T}_s^{1st}\right)^T \mathbf{K}^{1st} \left(\mathbf{T}_s^{1st}\right), \tag{12}$$

where $n_i = (i-1)$ for $i = 1, 2, 3, \ldots$. Based on a similar procedure, the global generalized force vector $\overline{\mathbf{f}}_s^{inn}$ can also be expressed in terms of $\mathbf{f}^{1st}$.

3. Coupling procedure

The coupling between FFEM and EFGM domains is accomplished by introducing interface elements between those domains (see Fig. 2). In these interface elements, a hybrid displacement approximation is defined that satisfies displacement continuity across the interface boundaries. For the detailed characteristics of interface elements, the papers [22, 23] can be referred. FE and EFG displacement approximations are briefly outlined before interface elements are described in detail. For displacement approximation in the Galerkin procedure, both FE and EFG use similar forms:

$$u_i^h(\mathbf{x}) = \sum_{I=1}^{n} \widetilde{\Phi}_I(\mathbf{x})\, d_{iI}, \tag{13}$$

where $u_i^h(\mathbf{x})$ is the nodal value of displacement component i at point $\mathbf{x}$, $\widetilde{\Phi}_I(\mathbf{x})$ are shape functions that depend on the method, and d_{iI} are the nodal parameters of displacement component i at node I.

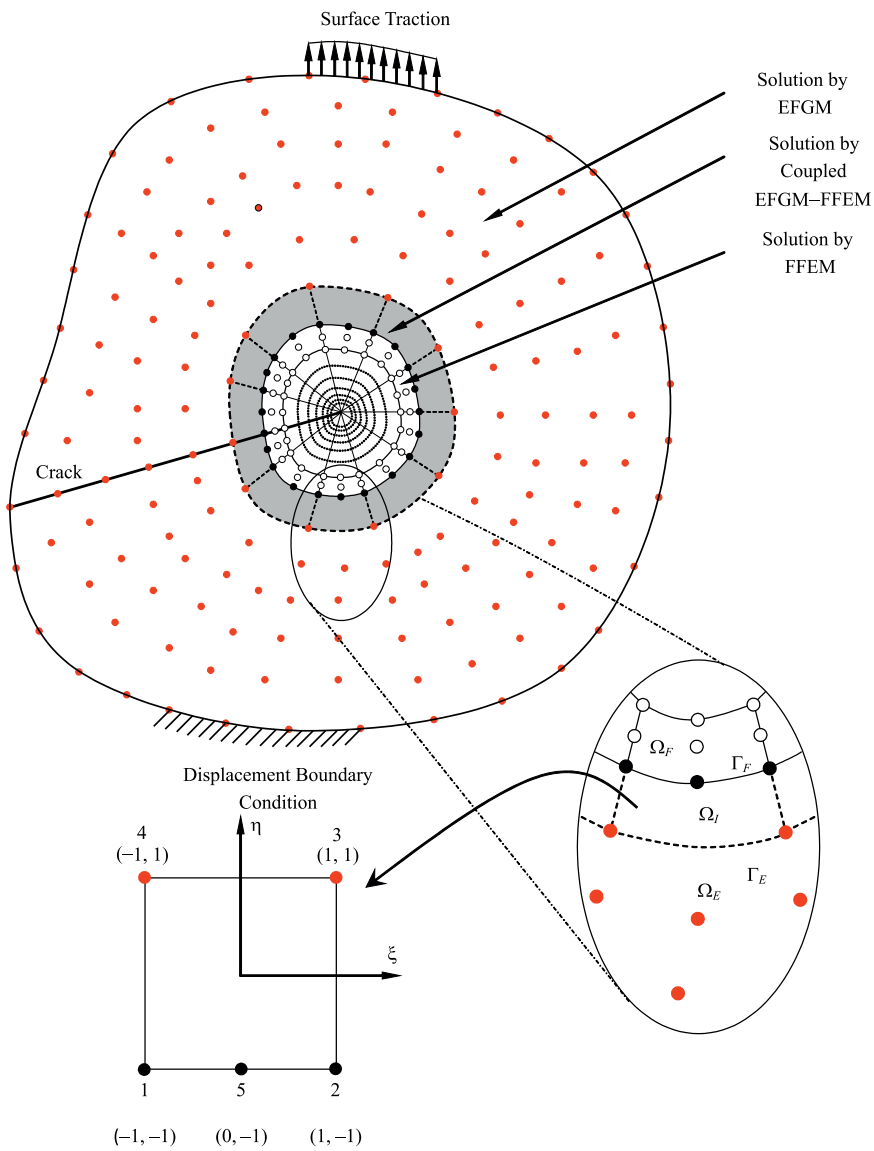

Fig. 2. Details of FFEM-EFGM coupling.

3.1. FE shape functions

The displacement approximation u_i, in an isoparametric element is given by

$$u_i^h(\mathbf{x}) = \sum_{I=1}^{n_{en}} N_I(\xi(\mathbf{x}))d_{iI}, \qquad \mathbf{x} \in \Omega_F^e, \tag{14}$$

where n_{en} is the number of element nodes. Because Q8 (8-node serendipity) and L9 (9-node Lagrangian) elements are used in FFEM discretization, in the present study a 5-node element is adopted for interface elements, the shape functions, $N_I(I = 1-5)$ of which in the parent domain ($\xi \in [-1,1], \eta \in [-1,1]$) (see Fig. 2) are as follows:

$$\begin{aligned} N_1 &= \frac{1}{4}\xi(\xi-1)(1-\eta), & N_2 &= \frac{1}{4}\xi(\xi+1)(1-\eta), \\ N_3 &= \frac{1}{4}\xi(\xi+1)(1+\eta), & N_4 &= \frac{1}{4}\xi(1-\xi)(1+\eta), \\ N_5 &= \frac{1}{2}(1-\xi^2)(1-\eta). \end{aligned} \tag{15}$$

3.2. EFG shape functions

In the EFG method, the displacement is approximated by moving least-squares approximations (MLS) [24]. The MLS approximation $u_i^h(\mathbf{x})$ is given by

$$u_i^h(\mathbf{x}) = \sum_{I=1}^{n} \Phi_I(\mathbf{x})d_{iI}, \qquad \mathbf{x} \in \Omega_E, \tag{16}$$

where n is the number of nodes in the neighborhood of $\mathbf{x}$, for which the weight function $w_I(\mathbf{x}) > 0$ and the EFG shape functions are defined as

$$\Phi_I(\mathbf{x}) = \sum_{J=1}^{m} p_J(\mathbf{x}) \left[\mathbf{A}^{-1}(\mathbf{x})\mathbf{C}(\mathbf{x})\right]_{JI}, \tag{17}$$

with $\mathbf{p}(\mathbf{x})$ being a vector of complete basis functions of order m, and $\mathbf{A}(\mathbf{x}) = \sum_{I=1}^{n} w_I(\mathbf{x})\mathbf{p}(\mathbf{x}_I)\mathbf{p}^T(\mathbf{x}_I)$ and $\mathbf{C}(\mathbf{x}) = [w_1(\mathbf{x})\mathbf{p}(\mathbf{x}_1), w_2(\mathbf{x})\mathbf{p}(\mathbf{x}_2), \ldots, w_n(\mathbf{x})\mathbf{p}(\mathbf{x}_n)]$.

In the present study, a linear basis in two dimensions, $\mathbf{p}^T(\mathbf{x}) = \{1, x_1, x_2\}$, $m = 3$ in conjunction with the following exponential weight function [19] is used,

$$w_I(\mathbf{x}) = w_I(r) = \begin{cases} \dfrac{e^{-(r/c)^2} - e^{-(1/c)^2}}{1 - e^{-(1/c)^2}} & 0 \le r \le 1 \\ 0 & r > 1 \end{cases}, \tag{18}$$

where c is a parameter that sets the relative weight inside the domain of influence (in the present study $c = 0.25$ is adopted), $r = z_I/z_{mI}$ with $z_I = ||\mathbf{x} - \mathbf{x_I}||$ being the distance from a sampling point $\mathbf{x}$ to a node $\mathbf{x}_I$, z_{mI} being the domain of influence of node I such that

$$z_{mI} = z_{\max} z_{cI}; \tag{19}$$

here z_{cI} is the characteristic nodal spacing distance which is chosen such that the node I has the number of neighbors sufficient for regularity of $\mathbf{A}(\mathbf{x})$ (which is used to determine the MLS approximation), and $z_{\max}$ is a scaling parameter.

3.3. Interface displacement approximation

A detailed schematic of interface domain is shown in Fig. 2. In Ω_E, the displacement at a point is approximated using the MLS approximants in Eq. (16), and in Ω_F, the FE interpolants in Eq. (14) are employed in each element subdomain Ω_F^e. In Ω_I, the interface region, the displacement at a point is approximated using the following expression:

$$u_i^h(\mathbf{x}) = u_i^{\mathrm{FE}}(\mathbf{x}) + R(\mathbf{x})\left[u_i^{\mathrm{EFG}}(\mathbf{x}) - u_i^{\mathrm{FE}}(\mathbf{x})\right] \equiv [1 - R(\mathbf{x})]\, u_I^{\mathrm{FE}}(\mathbf{x}) + R(\mathbf{x}) u_i^{\mathrm{EFG}}(\mathbf{x}), \qquad \mathbf{x} \in \Omega_l, \tag{20}$$

where u_i^{FE} and u_i^{EFG} are approximations for u_i, in Ω_I given by the FE and EFG approximations, respectively, and $R(\mathbf{x})$ is a ramp function [25] for coupling the FE and EFG regions. $R(\mathbf{x})$ is defined using the FE shape functions in Eq. 14:

$$R(\mathbf{x}) = \sum_{\substack{J \\ x_I \in \Gamma_E}} N_J(\mathbf{x}). \tag{21}$$

It can be verified that

$$R(\mathbf{x}) = \begin{cases} 1 & \mathbf{x} \in \Gamma_E \\ 0 & \mathbf{x} \in \Gamma_F \end{cases}, \tag{22}$$

and it varies linearly along interface element boundaries adjacent to other interface elements. Therefore, the approximation Eq. (20) reduces to u_i^{EFG} Eq. (16) on Γ_E and u_i^{FE} Eq. (14) on Γ_F, ensuring continuity. The interface shape functions can be developed by substituting the displacement approximations Eqs. (14) and (16) into Eq. (20):

$$u_i^h(\mathbf{x}) = [1 - R(\mathbf{x})] \sum_{I=1}^{n_{en}} N_I(\xi(\mathbf{x})) d_{iI} + R(\mathbf{x}) \sum_{I=1}^{n_{sn}} \Phi_I(\mathbf{x}) d_{iI} \equiv \sum_{I=1}^{n_{sn}} \overline{\Phi}_I(\mathbf{x}) d_{iI}, \qquad \mathbf{x} \in \Omega_I^e, \tag{23}$$

where the interface shape functions $\overline{\Phi}_I(\mathbf{x})$ are

$$\overline{\Phi}_I(\mathbf{x}) = \begin{cases} [1 - R(\mathbf{x})]\, N_I\left(\xi(\mathbf{x})\right) + R(\mathbf{x})\Phi_I(\mathbf{x}) & \mathbf{x}_I \in \Omega_I^e, \\ R(\mathbf{x})\Phi_I(\mathbf{x}) & \mathbf{x}_I \notin \Omega_I^e. \end{cases} \tag{24}$$

4. Variational formulation and discretization

For small displacements in two-dimensional, homogeneous, isotropic and linear-elastic solids, the equilibrium equations and boundary conditions are

$$\boldsymbol{\nabla} \cdot \boldsymbol{\sigma} + \mathbf{b} = \mathbf{0} \quad \text{in} \quad \Omega \tag{25}$$

and

$$\begin{aligned} \boldsymbol{\sigma} \cdot \mathbf{n} &= \overline{\mathbf{t}} \quad \text{on} \quad \Gamma_t \text{ (natural boundary conditions)}, \\ \mathbf{u} &= \overline{\mathbf{u}} \quad \text{on} \quad \Gamma_u \text{ (essential boundary conditions)}, \end{aligned} \tag{26}$$

respectively, where $\boldsymbol{\sigma} = \mathbf{D}\boldsymbol{\epsilon}$ is the stress vector, $\mathbf{D}$ is the material property matrix, $\boldsymbol{\epsilon} = \boldsymbol{\nabla}_s \mathbf{u}$ is the strain vector, $\mathbf{u}$ is the displacement vector, $\mathbf{b}$ is the body force vector, $\overline{\mathbf{t}}$ and $\overline{\mathbf{u}}$ are the vectors of prescribed surface tractions and displacements, respectively, $\mathbf{n}$ is a unit normal to the domain Ω, Γ_t and Γ_u are the portions of boundary, Γ where tractions and displacements are prescribed,

respectively, $\boldsymbol{\nabla}^T = \{\partial/\partial x_1, \partial/\partial x_2\}$ is the vector of gradient operators, and $\boldsymbol{\nabla}_s\mathbf{u}$ is the symmetric part of $\boldsymbol{\nabla}\mathbf{u}$.

Since the nodal parameters and the nodal displacements are the same in the finite elements, essential boundary conditions in the FFEM region can be applied by adopting the procedures similar to that in the FE analysis. In the following, the concept of application of essential boundary conditions in the EFGM and the transition regions is outlined. For an easy illustration, consider a single boundary constraint, $\overline{u}_i(\mathbf{x}_J) = g_i(\mathbf{x}_J)$ applied at node J (which belongs to the EFGM region or the transition region) in the direction of coordinate x_i. Then, the variational or weak form of Eqs. (25) and (26) can be expressed by

$$\int_{\Omega} \boldsymbol{\sigma}^T \delta\boldsymbol{\epsilon} d\Omega + f_i(\mathbf{x}_J)\delta u_i(\mathbf{x}_J) = \int_{\Omega} \mathbf{b}^T \delta\mathbf{u} d\Omega - \int_{\Gamma_t} \overline{\mathbf{t}}^T \delta\mathbf{u} d\Gamma, \tag{27}$$

$$\delta f_i(\mathbf{x}_J)\left[u_i(\mathbf{x}_J) - g_i(\mathbf{x}_J)\right] = 0, \tag{28}$$

where $f_i(\mathbf{x}_J)$ and $u_i(\mathbf{x}_J)$ are the ith component of $\mathbf{f}(\mathbf{x}_J)$ and $\mathbf{u}(\mathbf{x}_J)$, respectively. From Eqs. (13), (14), (16) and (23), the approximation of $u_i(\mathbf{x}_J)$ can be written as

$$u_i^h(\mathbf{x}_J) = \sum_{I=1}^{N} \widetilde{\Phi}_I(\mathbf{x}_J) d_{iI}, \tag{29}$$

where

$$\widetilde{\Phi}_I(\mathbf{x}) = \begin{cases} N_I\left(\xi(\mathbf{x})\right) & \mathbf{x} \in \Omega_F^e \\ \Phi_I(\mathbf{x}) & \mathbf{x} \in \Omega_E \\ \overline{\Phi}_I(\mathbf{x}) & \mathbf{x} \in \Omega_I^e \end{cases} \tag{30}$$

and N is the total number of nodal points in Ω. Using Eqs. (29) and (30) in the coupled FFEM-EFGM discretization (involving the master nodes (m), the slave nodes (s) and the nodes other than the master nodes (r)) of Eqs. (27) and (28) and application of the FFEM concepts outlined in Sec. 2, results in

$$\begin{bmatrix} \left\{\begin{matrix} \mathbf{K}_{rr}^R & \mathbf{K}_{rm}^R & \mathbf{0} \\ \mathbf{K}_{mr}^R & \mathbf{K}_{mm}^R + \mathbf{K}_{mm}^{1st} & \overline{\mathbf{K}}_{ms}^{1st} \\ \mathbf{0} & \overline{\mathbf{K}}_{sm}^{1st} & \overline{\mathbf{K}}_{ss}^{1st} + \overline{\mathbf{K}}_{s}^{inn} \end{matrix}\right\} & \widetilde{\boldsymbol{\Phi}}_J^i \\ \widetilde{\boldsymbol{\Phi}}_J^{iT} & 0 \end{bmatrix} \left\{\begin{Bmatrix} \mathbf{d}_r \\ \mathbf{d}_m \\ \mathbf{a} \end{Bmatrix} \atop f_i(\mathbf{x}_J)\right\} = \left\{\begin{Bmatrix} \mathbf{f}_r^R \\ \mathbf{f}_m^R + \mathbf{f}_m^{1st} \\ \overline{\mathbf{f}}_s^{1st} + \overline{\mathbf{f}}_s^{inn} \end{Bmatrix} \atop g_i(\mathbf{x}_J)\right\}, \tag{31}$$

where the submatrices and the subvectors in Eq. (31) are respectively obtained by partitioning and transforming the global stiffness matrix, whose the IJ-th component is given by

$$[\mathbf{K}]_{IJ} = \int_{\Omega} \mathbf{B}_I^T \mathbf{D} \mathbf{B}_J d\Omega \in \mathcal{L}\left(\Re^2 \times \Re^2\right), \tag{32}$$

and the global force vector whose I-th component is given by

$$[\mathbf{f}]_I = \int_{\Omega} \widetilde{\Phi}_I \mathbf{b}^T d\Omega - \int_{\Gamma_t} \widetilde{\Phi}_I \overline{\mathbf{t}}^T d\Gamma \in \Re^2. \tag{33}$$

In Eq. (32), $\mathbf{B}_I$ and $\mathbf{D}$ are respectively the strain displacement matrix and the linear elastic constitutive matrix.

In order to perform numerical integration in Eqs. (32) and (33), a background mesh is needed in the EFGM and in the transition regions. This background mesh can be independent of the arrangement of nodes; however, the nodes of the background mesh may coincide with the nodes in the EFGM and in the transition regions. In the present study, standard Gaussian quadrature is used to evaluate the integrals for assembling the stiffness matrix and the force vector by adopting 8×8 quadrature in the EFGM and in the transition regions. In the FFEM region, the integration order is varied from 2×2 to 4×4 quadrature to study its effect on the quality of the numerical solutions.

5. Essential boundary conditions

Lack of Kronecker's delta properties in the meshless shape functions, Φ_I poses some difficulties in imposing essential boundary conditions in the EFGM and in the transition regions. Nevertheless, several methods are currently available for enforcing essential boundary conditions. In this work, a full transformation method [26, 33] is adopted.

Consider the following transformation relating the nodal parameters and the nodal displacements of the master nodes (m), and the nodes other than the master nodes (r),

$$\left\{ \begin{array}{c} \widehat{\mathbf{d}}_r \\ \widehat{\mathbf{d}}_m \end{array} \right\} = \mathbf{\Lambda} \left\{ \begin{array}{c} \mathbf{d}_r \\ \mathbf{d}_m \end{array} \right\}, \tag{34}$$

where $\widehat{\mathbf{d}}_m$ and $\widehat{\mathbf{d}}_r$ are respectively the nodal displacements of the master nodes (m), and the nodes other than the master nodes (r), and

$$\mathbf{\Lambda} = \left[\begin{array}{cc} \overbrace{\left\{ \begin{array}{c} \widetilde{\mathbf{\Phi}}_1^{1T} \\ \widetilde{\mathbf{\Phi}}_1^{2T} \\ \widetilde{\mathbf{\Phi}}_2^{1T} \\ \widetilde{\mathbf{\Phi}}_2^{2T} \\ \vdots \end{array} \right\}}^{\substack{\text{nodes other than} \\ \text{master nodes in} \\ \text{regular region } (r)}} & \mathbf{0} \\ \mathbf{0} & \underbrace{\left\{ \begin{array}{ccccc} 1 & 0 & 0 & 0 & 0 \\ 0 & 1 & 0 & 0 & 0 \\ \vdots & \vdots & \ddots & \vdots & \vdots \\ 0 & 0 & 0 & 1 & 0 \\ 0 & 0 & 0 & 0 & 1 \end{array} \right\}}_{\text{master nodes } (r)} \end{array} \right] \in \mathcal{L}\left(\Re^{2(r+m)} \times \Re^{2(r+m)} \right), \tag{35}$$

is the transformation matrix. Note that along Γ_F which contains the master nodes (m), the interface shape functions $\overline{\Phi}_I(\mathbf{x})$ reduces to the finite element shape functions in Eq. (15). Multiplying the first two sets of matrix equations in Eq. (31) by $\mathbf{\Lambda}^{-T}$, one obtains

$$\begin{bmatrix} \left\{ \begin{array}{cc} \boldsymbol{\Lambda}^{-T} \left\{ \begin{array}{cc} \mathbf{K}_{rr} & \mathbf{K}_{rm} \\ \mathbf{K}_{mr} & \mathbf{K}_{mm} + \mathbf{K}_{mm}^{1st} \end{array} \right\} & \left\{ \begin{array}{c} \mathbf{0} \\ \overline{\mathbf{K}}_{ms}^{1st} \end{array} \right\} \\ \left\{ \mathbf{0} \quad \overline{\mathbf{K}}_{sm}^{1st} \right\} & \left\{ \overline{\mathbf{K}}_{ss}^{1st} + \overline{\mathbf{K}}_{s}^{inn} \right\} \end{array} \right\} & \left\{ \begin{array}{c} \boldsymbol{\Lambda}^{-T} \left\{ \begin{array}{c} \widetilde{\boldsymbol{\Phi}}_J^i \\ \mathbf{0} \end{array} \right\} \\ \mathbf{0} \end{array} \right\} \\ \left\{ \widetilde{\boldsymbol{\Phi}}_J^{iT} \quad \mathbf{0} \right\} \quad \mathbf{0} & 0 \end{bmatrix} \left\{ \begin{array}{c} \left\{ \begin{array}{c} \mathbf{d}_r \\ \mathbf{d}_m \\ \boldsymbol{a} \end{array} \right\} \\ f_i(\mathbf{x}_j) \end{array} \right\}$$

$$= \left\{ \begin{array}{c} \left\{ \begin{array}{c} \boldsymbol{\Lambda}^{-T} \left\{ \begin{array}{c} \mathbf{f}_r \\ \mathbf{f}_m + \mathbf{f}_m^{1st} \end{array} \right\} \\ \overline{\mathbf{f}}_s^{1st} + \overline{\mathbf{f}}_s^{inn} \end{array} \right\} \\ g_i(\mathbf{x}_J) \end{array} \right\}. \tag{36}$$

Exchanging the rows to replace the redundant equations by the constraint equation using the procedure outlined in [26, 33], leads to the following equation:

$$\mathcal{K} \left\{ \begin{array}{c} \mathbf{d}_r \\ \mathbf{d}_m \\ \boldsymbol{a} \end{array} \right\} = \mathcal{F}, \tag{37}$$

where $\mathcal{K}$ and $\mathcal{F}$ are the modified stiffness matrix and force vectors respectively. Using Eq. (37), $\{\mathbf{d}_r \quad \mathbf{d}_m \quad \boldsymbol{a}\}^T$ can be solved efficiently without needing any Lagrange multipliers. In the case of multiple boundary constraints, similar procedures are repeated. Knowing $\boldsymbol{a} = \{a_0, a_1, a_2, \ldots\}^T$, SIFs and T-stress can be calculated using Eqs. (3) and (4) respectively.

6. Numerical examples

Three numerical examples comprising of single edge crack tension (SECT), double edge crack tension (DECT) and center crack tension (CCT) are presented to illustrate the proposed coupled FFEM-EFGM. In Example 1, in order to check the numerical accuracy and stability, convergence studies on the estimates of K_I and T-stress using the proposed method are performed. The convergence is checked against Q8 and L9 fractal mesh configurations. The convergence study includes: (i) the effect of the scaling parameter $z_{\max}$ in the EFGM region on the solution; (ii) the effect of the integration order adopted in the FFEM region on the accuracy; (iii) the effect of the fractal mesh size on the accuracy; and (iv) the effect of different weight functions adopted in the EFGM region on the solution. The experience gained in the convergence study of Example 1 is used to analyze the problems presented in Examples 2–3. In all the numerical examples, elastic modulus E and Poisson's ratio ν are assumed to be 30×10^6 units and 0.25 respectively.

6.1. Example 1: Single Edge Crack Tension (SECT) Specimen

Consider a single edge crack tension specimen as shown in Fig. 3, that has length $2L = 3$ units, width $W = 1$ unit, and crack length $a = 0.5$ units. The far-field tensile stress, $\sigma = 1$ unit. Due to symmetry, only half of the plate is analyzed. Effect of both Q8 and L9 fractal mesh configurations on the estimates of K_I and T-stress are examined. Typical coupled FFEM-EFGM discretization with L9 fractal mesh configurations of rectangular and circular shapes having a similarity ratio ξ of 0.8, are shown in Figs. 4a and 4b respectively. The size of fractal mesh (distance from the crack tip to the curve Γ_0 on which the master nodes (m) are located) is $0.5a$. Plane stress condition is assumed. The number of fractal transformation terms used in $\mathbf{T}_s^{k\text{-}th}$ is 20. It can be easily verified that the discretization (shown in Figs. 4a and 4b) and the number of fractal transformation terms

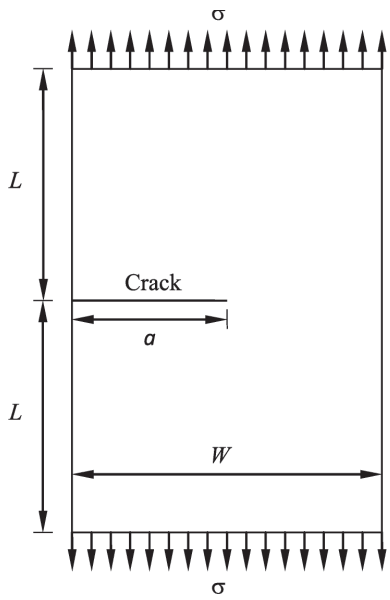

Fig. 3. Single edge crack tension specimen with geometry and loads.

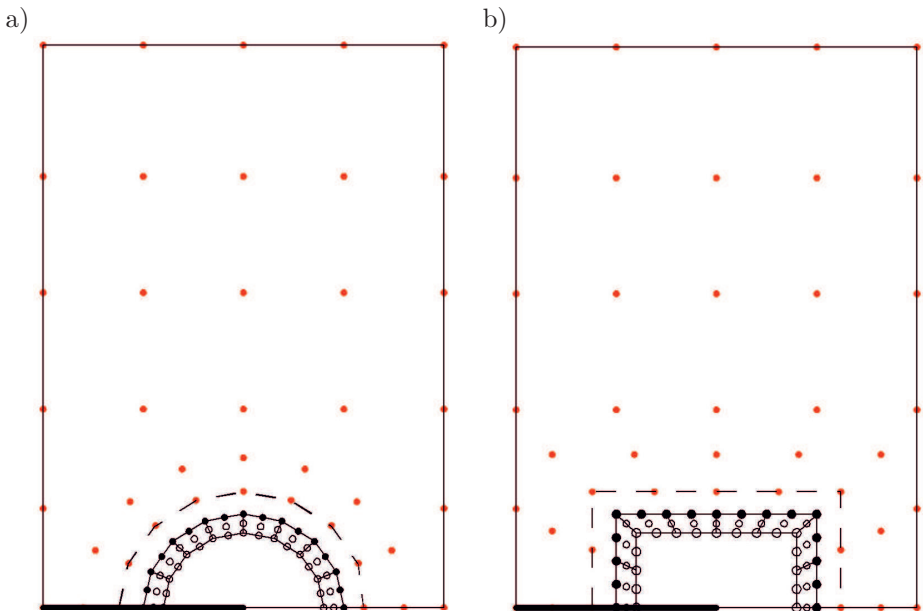

Fig. 4. Coupled FFEM-EFGM discretization with L9 fractal elements for single edge crack tension specimen: a) circular fractal mesh, b) rectangular fractal mesh.

adopted in the analysis, result in the total number of unknowns to be solved in Eq. (37) as 138. In the EFGM and the transition regions 8×8, Gaussian quadrature is adopted, whereas in the FFEM region the integration order is varied from 2×2 to 4×4 quadrature to study its effect on the quality of the numerical solutions. The analytical solution of K_I for SECT specimen given by Tada *et al.* [34], for different a/W ratios is as follows:

$$K_I = \sigma\sqrt{\pi a}\sqrt{\frac{2W}{\pi a}\tan\frac{\pi a}{2W}}\left[\frac{0.752 + 2.02\,(a/W) + 0.37\left(1 - \sin\dfrac{\pi a}{2W}\right)^3}{\cos\dfrac{\pi a}{2W}}\right]. \tag{38}$$

Similarly, the analytical solution of T-stress for SECT specimen with $L/W = 1.5$ is given by Fett [35], for different values a/W ratios.

Table 1 shows the results of parametric study carried out by varying the scaling parameter $z_{\max}$ in the EFGM region, using exponential weight function. In the FFEM region, the 2×2 Gaussian integration is used. It can be observed from Table 1 that for the discretization adopted (shown in Figs. 4a and 4b), $z_{\max} = 2.51$ along with L9 elements, provides accurate estimates of $K_I/(\sigma\sqrt{\pi a})$ and $T(1-a/W)^2/\sigma$ values, when compared with the benchmark solution of $K_I/(\sigma\sqrt{\pi a}) = 2.8266$ units [34] and $T(1-a/W)^2/\sigma = -0.106$ units [35].

Table 1. Effect of scaling parameter $z_{\max}$ value in EFGM region on predicted K_I and T-stress (Example 1).

Element type	Scaling parameter	$K_I/(\sigma\sqrt{\pi a})$		$T(1-a/W)^2/\sigma$	
		Proposed method	SIF ratio[a]	Proposed method	T-stress ratio[b]
Circular fractal mesh configuration					
L9	2.01	2.7729	0.9810	−0.1045	0.9858
L9	2.51	2.8319	1.0019	−0.1053	0.9934
L9	3.01	2.8459	1.0068	−0.1075	1.0142
Q8	2.01	2.7603	0.9765	−0.1039	0.9802
Q8	2.51	2.7661	0.9786	−0.1042	0.9830
Q8	3.01	2.9021	1.0267	−0.1079	1.0179
Rectangular fractal mesh configuration					
L9	2.01	2.7721	0.9807	−0.1043	0.9840
L9	2.51	2.8325	1.0021	−0.1050	0.9906
L9	3.01	2.8451	1.0065	−0.1071	1.0104
Q8	2.01	2.7412	0.9698	−0.1030	0.9717
Q8	2.51	2.7511	0.9733	−0.1037	0.9783
Q8	3.01	2.9031	1.0271	−0.1081	1.0198

[a] SIF ratio = ($K_I/(\sigma\sqrt{\pi a})$ by proposed method)/2.8266.

[b] T-stress ratio = ($T(1-a/W)^2/\sigma$ by proposed method)/−0.106.

The effect of the integration order adopted in the FFEM region on the quality of the estimates of $K_I/(\sigma\sqrt{\pi a})$ and $T(1-a/W)^2/\sigma$ is studied, using the coupled FFEM–EFGM discretization with fractal mesh configurations of rectangular and circular shapes, as shown in Figs. 4a and 4b respectively. The similarity ratio, the number of fractal transformation terms, the size of fractal mesh, and $z_{\max}$ are respectively 0.8, 20, $0.5a$ and 2.51. In the EFGM region, the exponential weight function is used. Table 2 presents the results of $K_I/(\sigma\sqrt{\pi a})$ and $T(1-a/W)^2/\sigma$ obtained using different integration orders in the FFEM region for fractal mesh configurations of rectangular and circular shapes. It can be observed from Table 2 that convergent and accurate estimates of $K_I/(\sigma\sqrt{\pi a})$ and $T(1-a/W)^2/\sigma$ can be obtained by adopting 2×2 Gaussian integration in the FFEM region.

Table 3 shows the effect of the nodal refinement in the EFGM region alone (keeping the discretization in FFEM region unchanged) on the predicted $K_I/(\sigma\sqrt{\pi a})$ and $T(1-a/W)^2/\sigma$ values, obtained using exponential weight function along with Q8 and L9 elements for fractal mesh configurations of rectangular and circular shapes. The similarity ratio, the number of fractal transformation terms, the size of fractal mesh and $z_{\max}$, are respectively 0.8, 20, $0.5a$ and 2.51. In the FFEM region 2×2 Gaussian integration is used. Table 3 also includes the details of the total number of unknowns to be solved in Eq. (37) for the discretization and the number of fractal transformation terms adopted. It can be observed from Table 3 that the nodal refinement in EFGM region alone has very small influence on the accuracy of $K_I/(\sigma\sqrt{\pi a})$ and $T(1-a/W)^2/\sigma$ estimates obtained using L9 elements, when compared with those obtained using Q8 elements. The convergence of the solutions with respect to the nodal refinement in the EFGM region alone, obtained by means of L9 elements shows more stability than those obtained using Q8 elements.

Table 2. Effect of integration order adopted in FFEM region on predicted K_I and T-stress (Example 1).

Element type	Order of integration	$K_I/(\sigma\sqrt{\pi a})$		$T(1-a/W)^2/\sigma$	
		Proposed method	SIF ratio[a]	Proposed method	T-stress ratio[b]
Circular fractal mesh configuration					
L9	2×2	2.8319	1.0019	−0.1053	0.9934
L9	3×3	2.8291	1.0009	−0.1052	0.9925
L9	4×4	2.8291	1.0009	−0.1052	0.9925
Q8	2×2	2.7661	0.9786	−0.1042	0.9830
Q8	3×3	2.7664	0.9787	−0.1043	0.9840
Q8	4×4	2.7664	0.9787	−0.1043	0.9840
Rectangular fractal mesh configuration					
L9	2×2	2.8325	1.0021	−0.1050	0.9906
L9	3×3	2.8293	1.0010	−0.1051	0.9915
L9	4×4	2.8293	1.0010	−0.1051	0.9915
Q8	2×2	2.7511	0.9733	−0.1037	0.9783
Q8	3×3	2.7535	0.9741	−0.1041	0.9821
Q8	4×4	2.7535	0.9741	−0.1041	0.9821

[a] SIF ratio = ($K_I/(\sigma\sqrt{\pi a})$ by proposed method)/2.8266.

[b] T-stress ratio = ($T(1-a/W)^2/\sigma$ by proposed method)/−0.106.

Table 3. Effect of nodal refinement in EFGM region on predicted K_I and T-stress (Example 1).

Element type	Number of EFGM nodes	Number of unknowns	$K_I/(\sigma\sqrt{\pi a})$		$T(1-a/W)^2/\sigma$	
			Proposed method	SIF ratio[a]	Proposed method	T-stress ratio[b]
Circular fractal mesh configuration						
L9	45	110	2.8463	1.0070	−0.1074	1.0132
L9	59	138	2.8319	1.0019	−0.1053	0.9934
L9	69	158	2.8251	0.9995	−0.1051	0.9915
L9	83	186	2.8249	0.9994	−0.1052	0.9925
Q8	45	110	2.7665	0.9787	−0.1079	1.0179
Q8	59	138	2.7661	0.9786	−0.1042	0.9830
Q8	69	158	2.7951	0.9889	−0.1048	0.9887
Q8	83	186	2.7804	0.9837	−0.1052	0.9925
Rectangular fractal mesh configuration						
L9	45	110	2.8592	1.0115	−0.1075	1.0142
L9	59	138	2.8325	1.0021	−0.1050	0.9906
L9	69	158	2.8321	1.0019	−0.1052	0.9925
L9	83	186	2.8346	1.0028	−0.1051	0.9915
Q8	45	110	2.7465	0.9717	−0.1021	0.9632
Q8	59	138	2.7511	0.9733	−0.1037	0.9783
Q8	69	158	2.7791	0.9832	−0.1032	0.9736
Q8	83	186	2.7801	0.9835	−0.1035	0.9764

[a] SIF ratio = ($K_I/(\sigma\sqrt{\pi a})$ by proposed method)/2.8266.

[b] T-stress ratio = ($T(1-a/W)^2/\sigma$ by proposed method)/−0.106.

Using the proposed method, the effect of the fractal mesh size is studied, using the coupled FFEM-EFGM discretization with fractal mesh configurations of rectangular and circular shapes similar to that shown in Figs. 4a and 4b respectively. The similarity ratio, the number of fractal transformation terms and $z_{\max}$, are respectively 0.8, 20, and 2.51. In the FFEM region, the 2×2 Gaussian integration is used. In the EFGM region exponential weight function is used. Table 4 shows the results of $K_I/(\sigma\sqrt{\pi a})$ and $T(1-a/W)^2/\sigma$, obtained using Q8 and L9 elements for fractal mesh configurations of rectangular and circular shapes. It can be observed from Table 4 that the results are insensitive to the fractal mesh sizes in combination with the similarity ratio, the number of fractal transformation terms, and the similarity ratio considered in the present study. In addition, from Table 4 it can be observed that the estimates of $K_I/(\sigma\sqrt{\pi a})$ and $T(1-a/W)^2/\sigma$ obtained using L9 elements are more accurate when compared with those obtained using Q8 elements.

Table 4. Effect of fractal mesh size on predicted K_I and T-stress (Example 1).

Element type	Size of fractal domain	$K_I/(\sigma\sqrt{\pi a})$		$T(1-a/W)^2/\sigma$	
		Proposed method	SIF ratio[a]	Proposed method	T-stress ratio[b]
Circular fractal mesh configuration					
L9	0.25	2.8181	0.9970	−0.1062	1.0019
L9	0.5	2.8319	1.0019	−0.1053	0.9934
L9	0.75	2.8152	0.9960	−0.1054	0.9943
Q8	0.25	2.7523	0.9737	−0.1082	1.0208
Q8	0.5	2.7661	0.9786	−0.1042	0.9830
Q8	0.75	2.9134	1.0307	−0.1046	0.9868
Rectangular Fractal Mesh Configuration					
L9	0.25	2.8318	1.0018	−0.1054	0.9943
L9	0.5	2.8325	1.0021	−0.1050	0.9906
L9	0.75	2.8108	0.9944	−0.1051	0.9915
Q8	0.25	2.7359	0.9679	−0.1031	0.9726
Q8	0.5	2.7511	0.9733	−0.1037	0.9783
Q8	0.75	2.8019	0.9913	−0.1031	0.9726

[a] SIF ratio = ($K_I/(\sigma\sqrt{\pi a})$ by proposed method)/2.8266.

[b] T-stress ratio = ($T(1-a/W)^2/\sigma$ by proposed method)/−0.106.

Using the proposed method, the effect of the similarity ratio on the predicted $K_I/(\sigma\sqrt{\pi a})$ and $T(1-a/W)^2/\sigma$ values is studied by varying the similarity ratio ξ from 0.1 to 0.9, using the coupled FFEM-EFGM discretization with fractal mesh configurations of rectangular and circular shapes similar to those shown in Figs. 4a and 4b respectively. The number of fractal transformation terms, the size of fractal mesh and $z_{\max}$, are respectively 20, $0.5a$ and 2.51. In the FFEM region 2×2 Gaussian integration is used. In the EFGM region exponential weight function is used. Figures 5a and 5b show respectively the convergence of SIF ratio ($K_I/(\sigma\sqrt{\pi a})$ by the proposed method/2.8266) and T-stress ratio ($T(1-a/W)^2/\sigma$ by the proposed method/−0.106) estimates with the similarity ratio ξ employed, for fractal mesh configurations of rectangular and circular shapes respectively. It can be observed from Figs. 5a and 5b that accuracy increases with the similarity ratio. This is quite natural, because finer fractal meshes will be generated for higher value of similarity ratios and therefore will give better results. However, when very high value of similarity ratio is used, numerical errors arise and cause large discrepancies. It can be observed from Figs. 5a and 5b that L9 elements produce better results when compared with those obtained using Q8 elements.

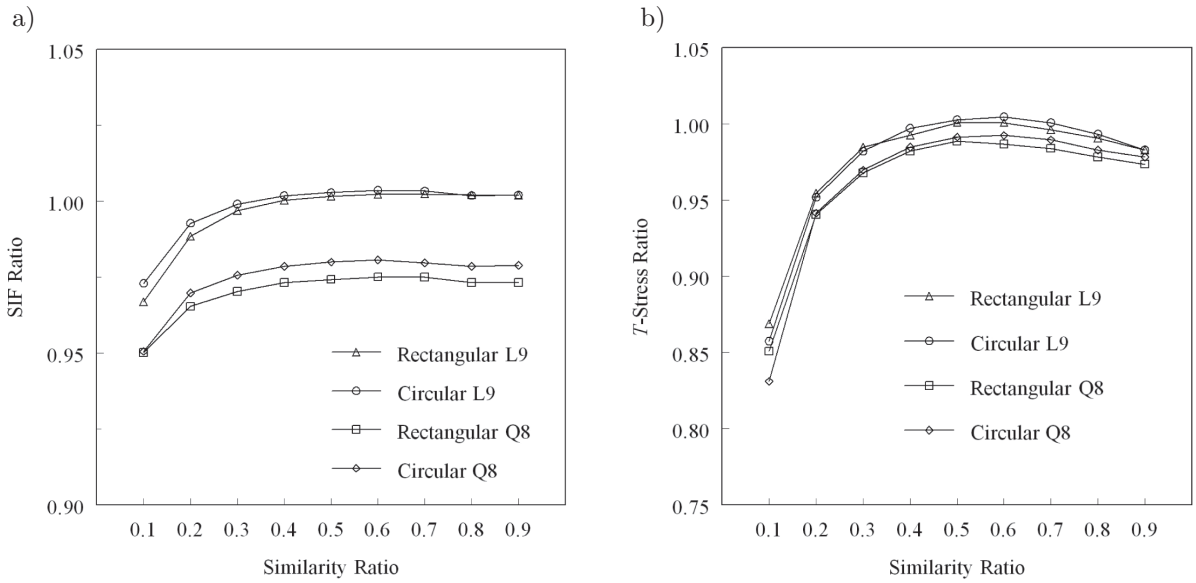

Fig. 5. Effect of similarity ratio (Example 1): a) convergence of K_I, b) convergence of T-stress.

Using the proposed method, the effect of the number of fractal transformation terms on the predicted $K_I/(\sigma\sqrt{\pi a})$ and $T(1-a/W)^2/\sigma$ values is studied, by varying the number of fractal transformation terms used in $\mathbf{T}_s^{k\text{-}th}$ from 4 to 24. Coupled FFEM-EFGM discretization with fractal mesh configurations of rectangular and circular shapes, as shown in Figs. 4a and 4b respectively, is adopted. The similarity ratio, the size of fractal mesh and $z_{\max}$ are respectively 0.8, $0.5a$ and 2.51. In the FFEM region 2×2 Gaussian integration is used. In the EFGM region exponential weight function is used. Figures 6a and 6b show respectively the convergence of SIF ratio and T-stress ratio estimates with the number of fractal transformation terms used, for fractal mesh configurations of rectangular and circular shapes, respectively. It can be observed from Figs. 6a and 6b that L9 elements produce better results when compared with those obtained using the Q8 elements.

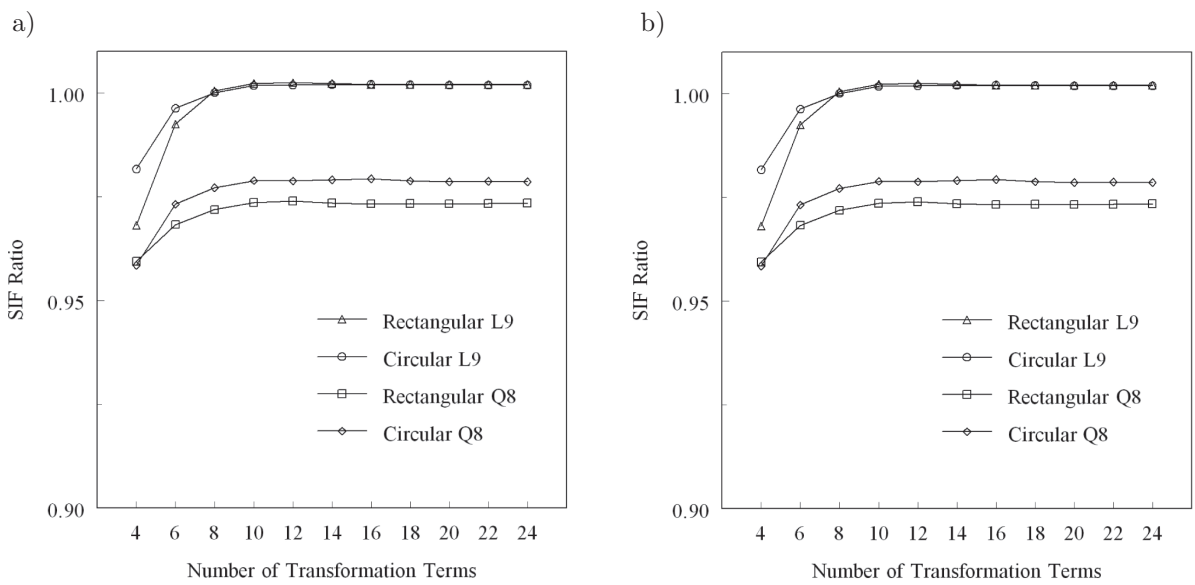

Fig. 6. Effect of number of fractal transformation terms (Example 1); a) convergence of K_I, b) convergence of T-stress.

For crack length-to-width ratio $a/W = 0.5$, the angular variations of the stress components σ_{rr}, $\sigma_{\theta\theta}$, and shear stress, $\tau_{r\theta}$ at radial distance to crack length $r/a = 0.01$, are shown in Fig. 7. Coupled

FFEM-EFGM discretization with L9 fractal mesh configurations of rectangular and circular shapes, as shown in Figs. 4a and 4b respectively, is used. The similarity ratio, the number of fractal transformation terms, the size of fractal mesh, and $z_{\max}$, are respectively 0.8, 20, 0.5a and 2.51. In the FFEM region 2×2 Gaussian integration is used. In the EFGM region, exponential weight function is used. Figure 7 also includes the plots of exact stresses from the LEFM singularity field near the crack tip [36], obtained by using the benchmark solution of $K_I/\left(\sigma\sqrt{\pi a}\right) = 2.8266$ units [34]. The stresses predicted by the proposed method match very well with the exact stresses.

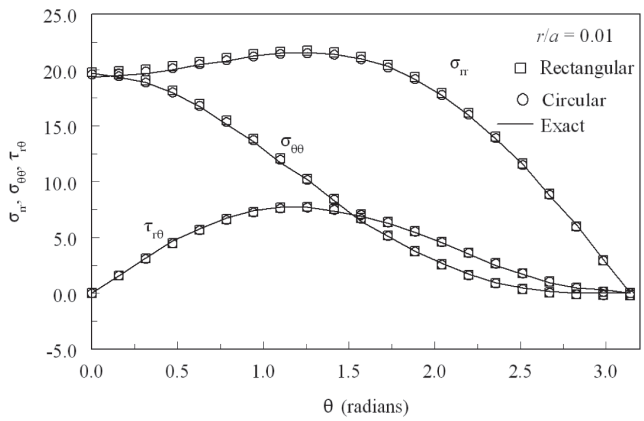

Fig. 7. Angular variations of σ_{rr}, $\sigma_{\theta\theta}$, and $\tau_{r\theta}$ (Example 1).

The effect of a/W ratio on the estimates of $K_I/\left(\sigma\sqrt{\pi a}\right)$ and $T\left(1-a/W\right)^2/\sigma$ is studied, using the coupled FFEM-EFGM discretization, with fractal mesh configurations of rectangular and circular shapes similar to that shown in Figs. 4a and 4b respectively. The similarity ratio, the number of fractal transformation terms and $z_{\max}$, are respectively 0.8, 20, and 2.51. The size of fractal mesh for $a/W = 0.1 - 0.5,\ 0.6,\ 0.7,\ 0.8$, and 0.9 are respectively 0.5a, 0.333a, 0.214a, 0.125a, and 0.056a. In the FFEM region, 2×2 Gaussian integration is used. In the EFGM region, exponential weight function is used. Figures 8a and 8b show respectively the estimates of $K_I/\left(\sigma\sqrt{\pi a}\right)$ and $T\left(1-a/W\right)^2/\sigma$ as a function of a/W ratio, obtained using Q8 and L9 elements for fractal mesh configurations of rectangular and circular shapes. Figures 8a and 8b demonstrate that the estimates of $K_I\left(\sigma\sqrt{\pi a}\right)$ and $T\left(1-a/W\right)^2/\sigma$ as a function of a/W ratio obtained using the proposed method are in good agreement with the benchmark solutions of $K_I/\left(\sigma\sqrt{\pi a}\right)$ [34] and $T\left(1-a/W\right)^2/\sigma$ [35].

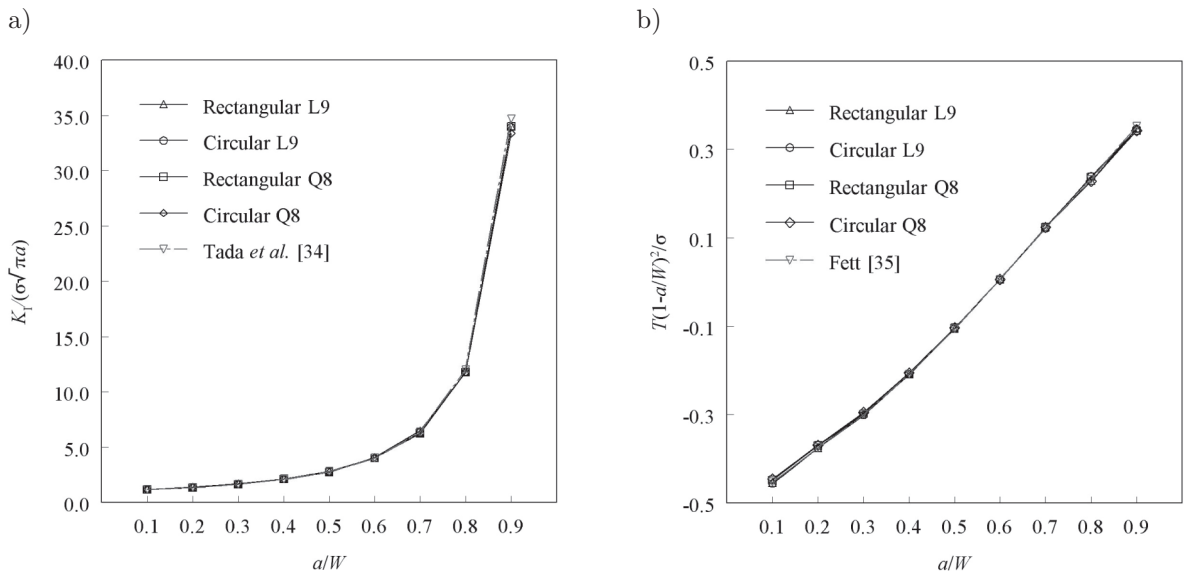

Fig. 8. Effect of a/W ratio (Example 1); a) K_I, b) T-stress.

6.2. Example 2: Double Edge Crack Tension (DECT) Specimen

Consider a double edge crack tension specimen as shown in Fig. 9, that has length $2L = 3$ units, width $W = 1$ unit, and crack length $a = 0.5$ units. Due to symmetry, only a quarter of the plate is analyzed. Coupled FFEM-EFGM discretization and other parameters are same as those used in Example 1. The analytical solution of K_I for DECT specimen given by Leung and Su [3], for different a/W ratios is as follows:

$$K_I = \sigma\sqrt{\pi a}\left[\frac{1.12 - 0.61\,(a/W) + 0.13\,(a/W)^3}{\sqrt{(1 - a/W)}}\right]. \tag{39}$$

Similarly, the analytical solution of T-stress for DECT specimen with $L/W = 1.5$ is given by Fett [35], for different a/W ratios.

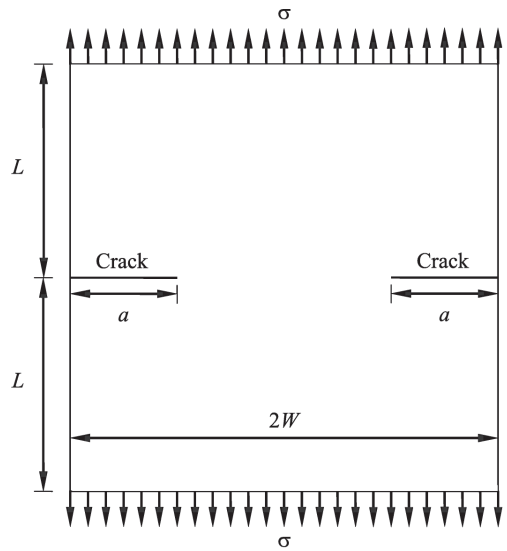

Fig. 9. Double edge crack tension specimen with geometry and loads.

Figures 10a and 10b shows respectively the convergence of SIF ratio ($K_I/(\sigma\sqrt{\pi a})$ by the proposed method/1.1756) and T-stress ratio (T/σ by proposed method/-0.522) estimates with the

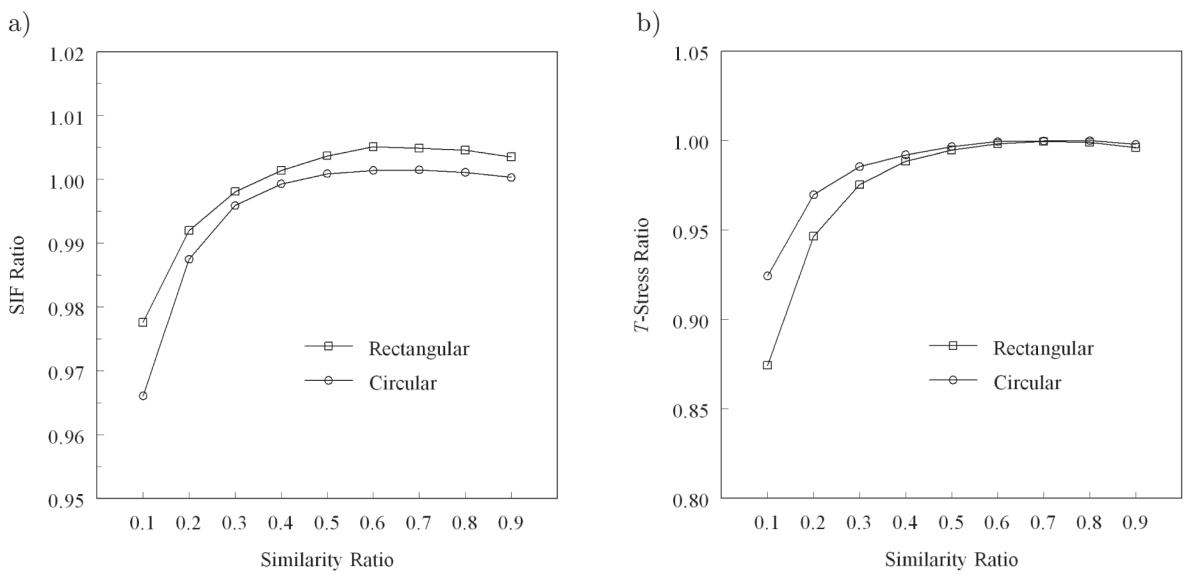

Fig. 10. Effect of similarity ratio (Example 2); a) convergence of K_I, b) convergence of T-stress.

similarity ratio ξ employed, obtained using L9 elements for fractal mesh configurations of rectangular and circular shapes. It can be observed from Figs. 10a and 10b that accuracy increases with similarity ratio and that the circular fractal mesh configurations produce slightly better results when compared with those obtained using the rectangular mesh configurations.

Figures 11a and 11b show respectively the convergence of SIF ratio and T-stress ratio estimates with the number of fractal transformation terms used, obtained using L9 elements for fractal mesh configurations of rectangular and circular shapes. It can be observed from Figures 11(a) and 11(b) that the circular fractal mesh configurations produce slightly better results when compared with those obtained using the rectangular mesh configurations.

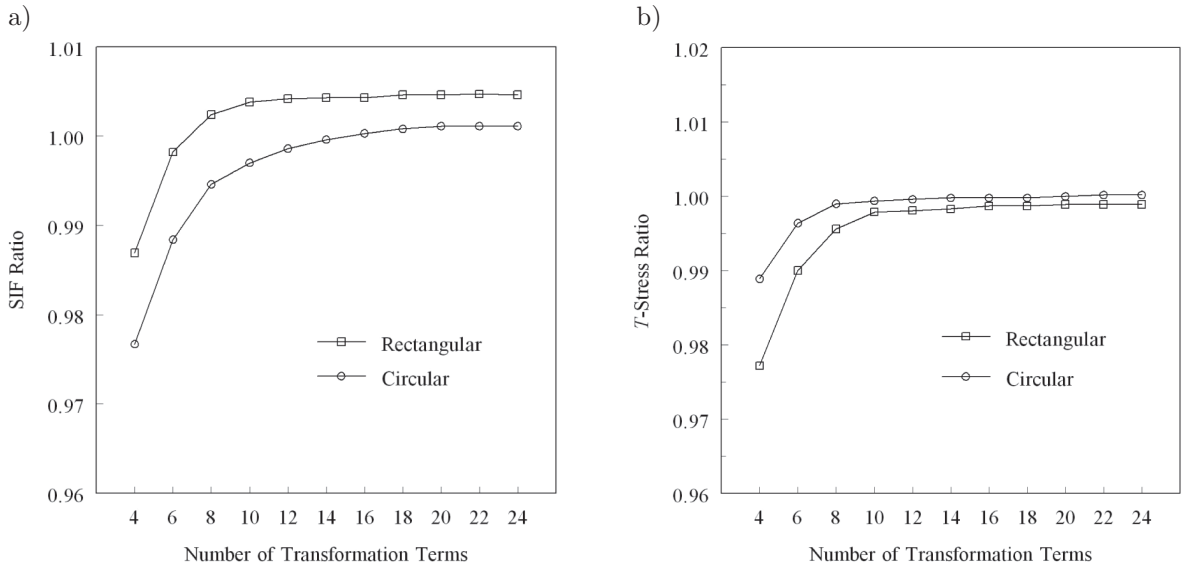

Fig. 11. Effect of number of fractal transformation terms (Example 2); a) convergence of K_I, b) convergence of T-stress.

For crack length-to-width ratio $a/W = 0.5$, the angular variations of the stress components σ_{rr}, $\sigma_{\theta\theta}$, and shear stress, $\tau_{r\theta}$ at radial distance to crack length $r/a = 0.01$, are shown in Fig. 12. Figure 12 also include the plots of exact stresses from the LEFM singularity field near the crack tip [36], obtained by using the benchmark solution of $K_I/(\sigma\sqrt{\pi a}) = 1.1756$ units [3]. The predicted stresses from the proposed method match very well the exact stresses.

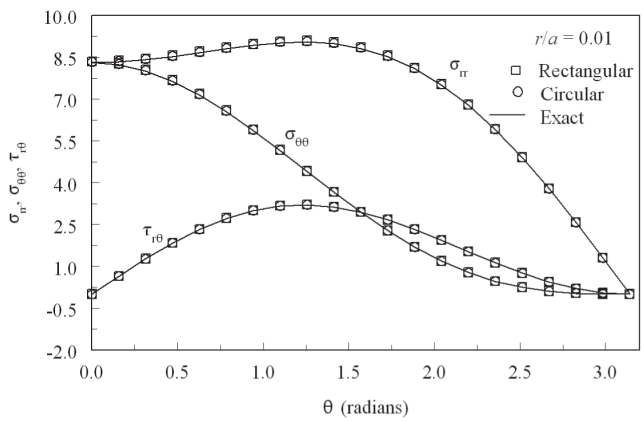

Fig. 12. Angular variations of σ_{rr}, $\sigma_{\theta\theta}$, and $\tau_{r\theta}$ (Example 2).

Figures 13a and 13b show respectively the estimates of $K_I/(\sigma\sqrt{\pi a})$ and T/σ as a function of a/W ratio, obtained using L9 elements for fractal mesh configurations of rectangular and circular

shapes. Figures 13a and 13b demonstrate that the estimates of $K_I/(\sigma\sqrt{\pi a})$ and T/σ as functions of a/W ratio obtained using the proposed method, are in good agreement with the benchmark solutions of $K_I/(\sigma\sqrt{\pi a})$ [3] and T/σ [35].

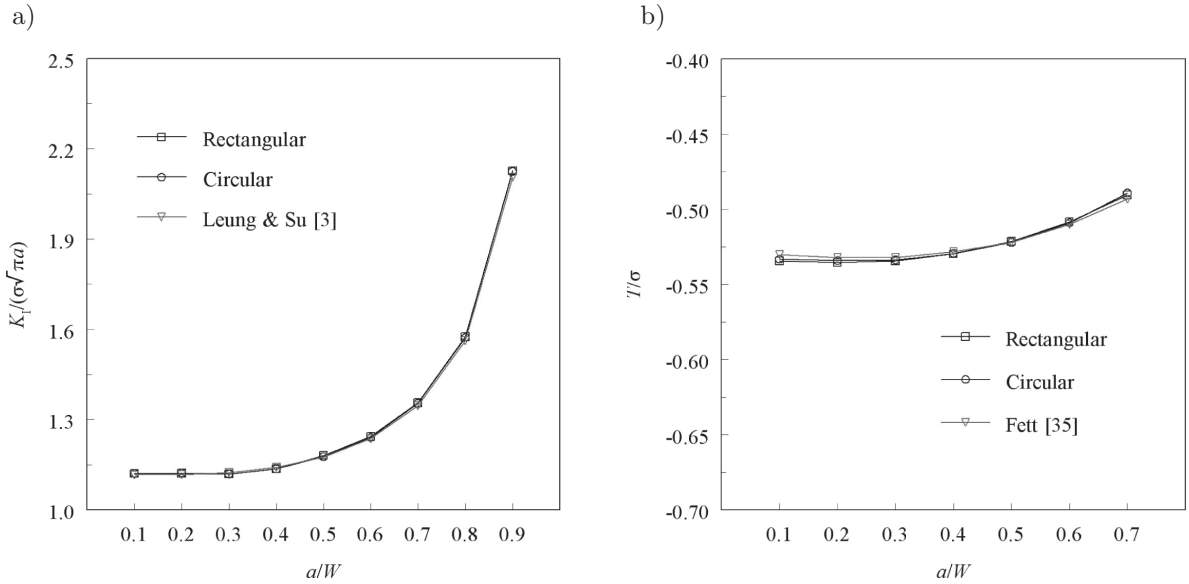

Fig. 13. Effect of a/W ratio (Example 2); a) K_I, b) T-stress.

6.3. Example 3: Center Crack Tension (CCT) Specimen

Consider a center crack tension specimen as shown in Fig. 14, that has length $2L = 3$ units, width $W = 1$ unit, and crack length $a = 0.5$ units. Due to symmetry, only a quarter of the plate is analyzed. Coupled FFEM-EFGM discretization and other parameters are the same as those used in Example 2. The analytical solution of K_I for CCT specimen given by Benthem and Koiter [37], for different a/W ratios, is as follows:

$$K_I = \sigma\sqrt{\pi a}\left[\frac{1.0 - 0.5\,(a/W) + 0.326\,(a/W)^2}{\sqrt{(1 - a/W)}}\right]. \tag{40}$$

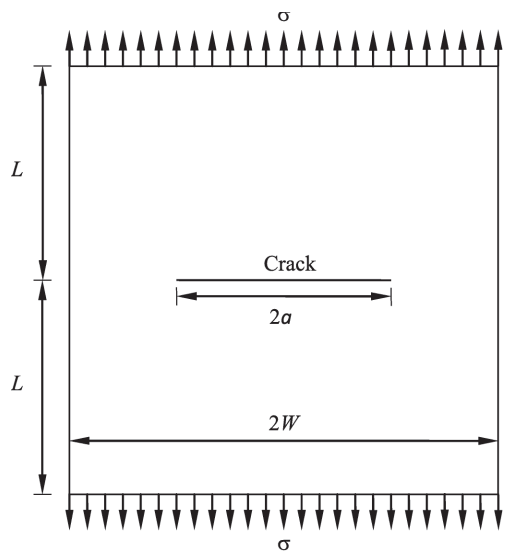

Fig. 14. Centre crack tension specimen with geometry and loads.

Similarly, the analytical solution of T-stress for CCT specimen with $L/W = 1.5$ can be obtained from Fett [35].

Figures 15a and 15b show respectively the convergence of SIF ratio ($K_I/(\sigma\sqrt{\pi a})$ by the proposed method/1.1759) and T-stress ratio ($T\,(1 - a/W)\,/\sigma$ by the proposed method/-0.6236) estimates with the similarity ratio ξ employed, obtained using L9 elements for fractal mesh configurations of rectangular and circular shapes. It can be observed from Figs. 15a and 15b that accuracy increases with the similarity ratio and that the circular fractal mesh configurations produce slightly better results when compared with those obtained using the rectangular mesh configurations.

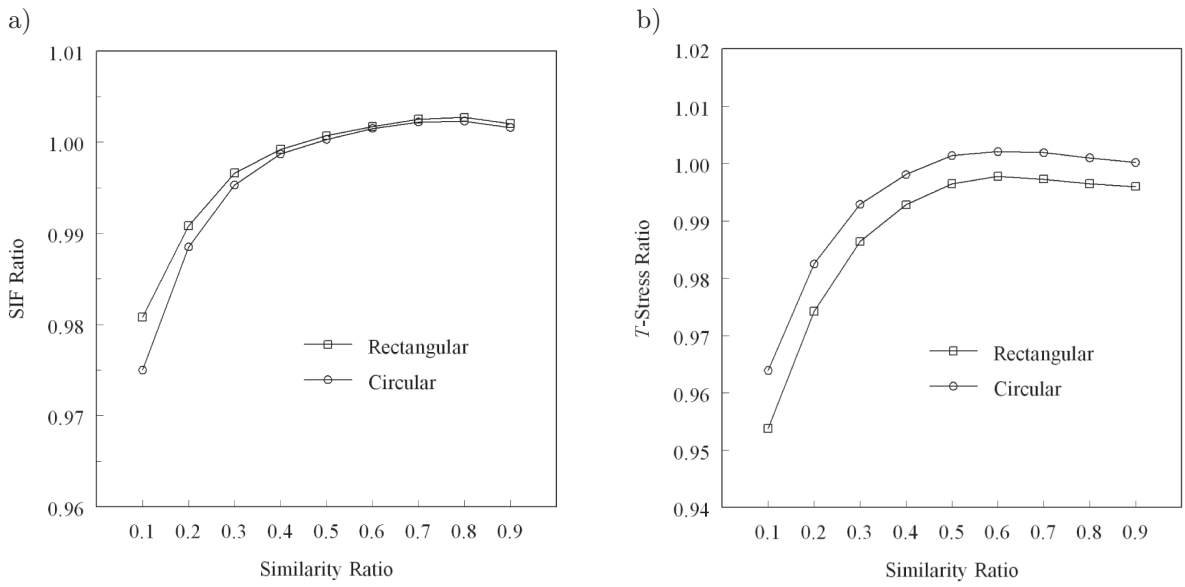

Fig. 15. Effect of similarity ratio (Example 3); a) convergence of K_I, b) convergence of T-stress.

Figures 16a and 16b show respectively the convergence of SIF ratio and T-stress ratio estimates with the number of fractal transformation terms used, obtained using L9 elements for fractal mesh

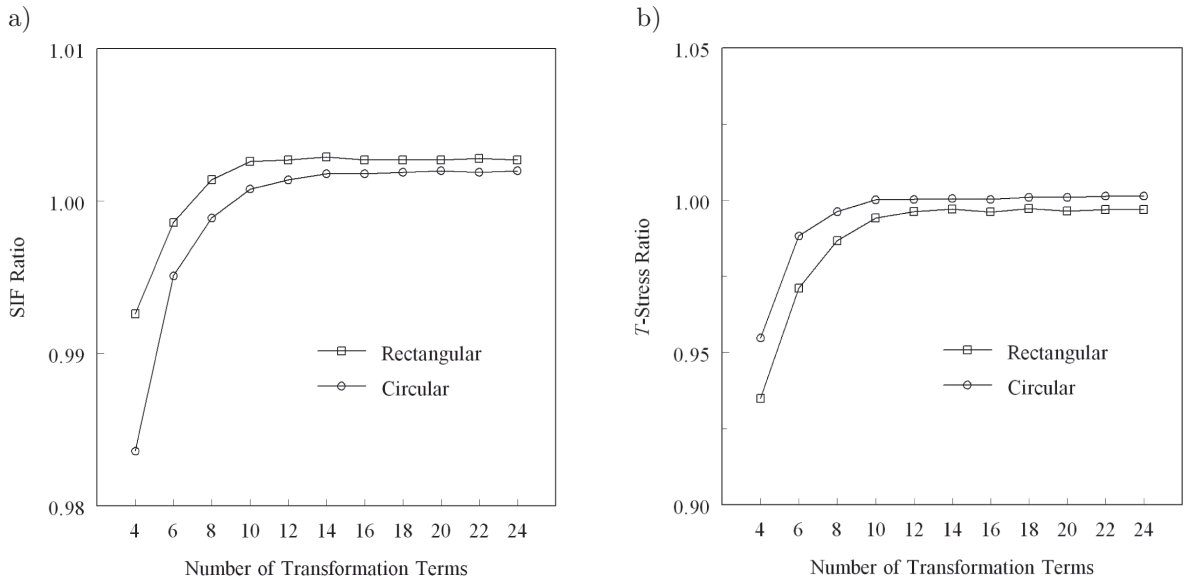

Fig. 16. Effect of number of fractal transformation terms (Example 3); a) convergence of K_I, b) convergence of T-stress.

configurations of rectangular and circular shapes. It can be observed from Figs. 16a and 16b that the circular fractal mesh configurations produce slightly better results when compared with those obtained using the rectangular mesh configurations.

For crack length-to-width ratio $a/W = 0.5$, the angular variations of the stress components σ_{rr}, $\sigma_{\theta\theta}$, and shear stress, $\tau_{r\theta}$ at radial distance to crack length $r/a = 0.01$, are shown in Fig. 17. Figure 17 also includes the plots of exact stresses from the LEFM singularity field near the crack tip [36], obtained by using the benchmark solution of $K_I/(\sigma\sqrt{\pi a}) = 1.1759$ units [37]. The predicted stresses from the proposed method match very well the exact stresses.

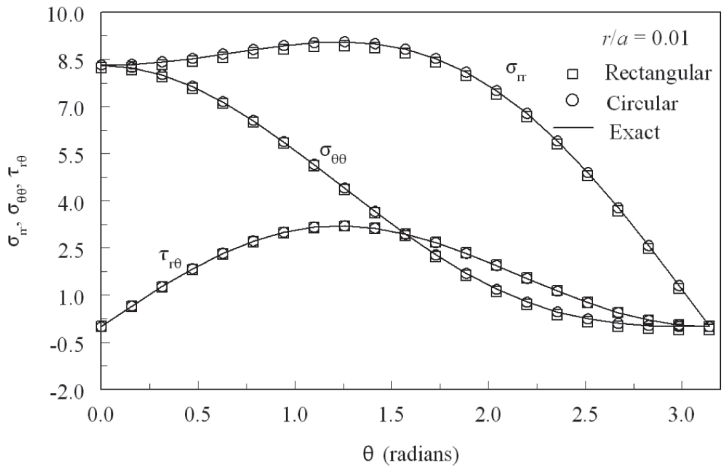

Fig. 17. Angular variations of σ_{rr}, $\sigma_{\theta\theta}$, and $\tau_{r\theta}$ (Example 3).

Figures 18a and 18b show respectively the estimates of $K_I/(\sigma\sqrt{\pi a})$ and $T(1-a/W)/\sigma$ as functions of a/W ratio, obtained using L9 elements for fractal mesh configurations of rectangular and circular shapes. Figures 18a and 18b demonstrate that the estimates of $K_I/(\sigma\sqrt{\pi a})$ and $T(1-a/W)/\sigma$ as functions of a/W ratio obtained using the proposed method are in good agreement with the benchmark solutions of $K_I/(\sigma\sqrt{\pi a})$ [37] and $T(1-a/W)/\sigma$ [35].

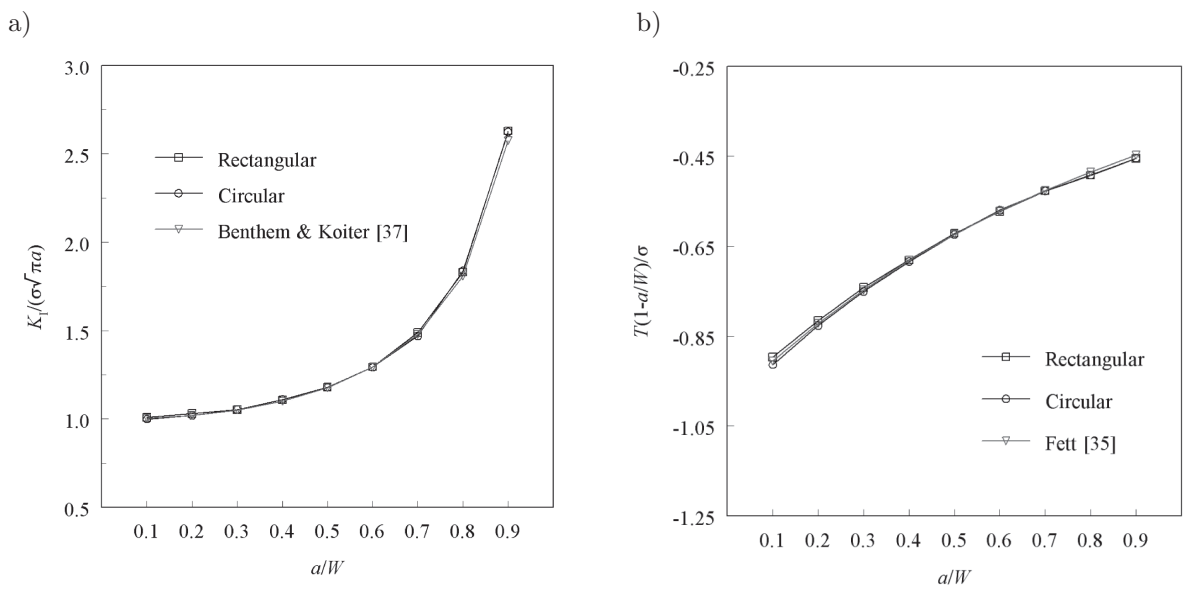

Fig. 18. Effect of number of fractal transformation terms (Example 3); a) convergence of K_I, b) convergence of T-stress.

7. Summary and conclusions

This paper presents a coupling technique for integrating FFEM with EFGM for analyzing homogeneous, isotropic, and two-dimensional linear-elastic cracked structures subjected to Mode I loading condition. FFEM is adopted for discretization of domain close to the crack tip and EFGM is adopted in the rest of the domain. In the transition region interface elements are employed. The interface element shape functions which comprise both the element-free Galerkin and the finite element shape functions, satisfy the consistency condition, thus ensuring convergence of the proposed coupled FFEM-EFGM. The proposed method combines the best features of FFEM and EFGM, in the sense that no structured mesh or special enriched basis functions are necessary and no post-processing (employing any path-independent integrals) is needed to determine fracture parameters such as SIFs and T-stress. Three numerical examples are presented to illustrate the proposed method by calculating SIFs and T-stress. The convergence is checked against Q8 and L9 fractal mesh configurations. The convergence study includes: (i) the effect of the scaling parameter $z_{\max}$ in the EFGM region on the solution; (ii) the effect of the integration order adopted in the FFEM region on the accuracy; (iii) the effect of the fractal mesh size on the accuracy; and (iv) the effect of different weight functions adopted in the EFGM region on the solution.

The present study indicates that using the proposed coupled FFEM-EFGM, convergent and accurate solutions can be obtained by adopting an exponential weight function along with the scaling parameter equal to 2.51, 2×2 Gaussian integration in the FFEM region, the number of fractal transformation terms equal to 20, and the similarity ratio equal to 0.8. The results are insensitive to the fractal mesh sizes in combination with the similarity ratio, the number of fractal transformation terms, and the similarity ratio considered in the present study. The nodal refinement in EFGM region alone has very little influence on the accuracy of solutions obtained using L9 elements, when compared with those obtained using Q8 elements. The convergence of the solutions with respect to the nodal refinement in the EFGM region alone, obtained using L9 elements, shows more stability than those obtained using Q8 elements. It is observed that L9 elements produce better results when compared with those obtained using Q8 elements. The predicted LEFM stress singularity field near the crack tip stresses from the proposed coupled FFEM-EFGM using L9 elements, match very well the exact stresses. The estimates of SIFs and T-stress obtained as a function of a/W ratio using the proposed method are in good agreement with the benchmark solutions. Numerical examples based on Mode-I deformations show that the circular fractal mesh configurations produce slightly better results when compared with those obtained using the rectangular mesh configurations.

References

[1] C.B. Hu, Y.T. Li, J. Gong. The Transition Method of Geometrically Similar Element for Dynamic Crack Problem. *Key Engineering Materials*, **145–149** (Part 1): 267–272, 1998.

[2] C.M. Song, J.P. Wolf. Semi-Analytical Representation of Stress Singularities as Occurring in Cracks in Anisotropic Multi-Materials with the Scaled Boundary Finite-Element Method. *Computers & Structures*, **80**: 83–197, 2002.

[3] A.Y.T. Leung, R.K.L. Su. Mode I Crack Problems by Fractal Two−Level Finite Element Methods. *Engineering Fracture Mechanics*, **48**(6): 847–856, 1994.

[4] A.Y.T. Leung, R.K.L. Su. Mixed Mode Two-Dimensional Crack Problems by Fractal Two-Level Finite Element Method. *Engineering Fracture Mechanics*, **51**(6): 889–895, 1995.

[5] A.Y.T. Leung, R.K.L. Su. Two-Level Finite Element Study of Axisymmetric Cracks. *International Journal of Fracture*, **89**(2): 193–203, 1998.

[6] A.Y.T. Leung, R.K.L. Su. Applications of Fractal Two-Level Finite Element Method for 2D Cracks. *Microcomputers in Civil Engineering*, **11**(4): 249–257, 1996.

[7] A.Y.T. Leung, R.K.L. Su. Fractal Two-Level Finite Element Method for Cracked Kirchhoff's Plates using DKT Elements. *Engineering Fracture Mechanics*, **54**(5): 703–711, 1996.

[8] A.Y.T. Leung, R.K.L. Su. Fractal Two-Level Finite Element Analysis of Cracked Reissner's Plate. *Thin-Walled Structures*, **24**(4): 315–334, 1996.

[9] R.K.L. Su, A.Y.T. Leung. Mixed Mode Cracks in Reissner Plates. *International Journal of Fracture*, **107**(3): 235–257, 2001.

[10] R.K.L. Su, H.Y. Sun Numerical Solution of Cracked Thin Plates Subjected to Bending, Twisting and Shear Loads. *International Journal of Fracture*, **117**(4): 323–335, 2002.
[11] A.Y.T. Leung, R.K.L. Su. Eigenfunction Expansion for Penny-Shaped and Circumferential Cracks. *International Journal of Fracture*, **89**(3): 205–222, 1998.
[12] Leung, A.Y.T., and Su, R.K.L., Fractal Two-Level Finite Element Method for Free Vibration of Cracked Beams. *Journal of Shock and Vibration*, Vol. 5 (**??**), pp. 61–68, 1998.
[13] A.Y.T. Leung, R.K.L. Su. A Numerical Study of Singular Stress Field of 3-D Cracks. *Finite Elements in Analysis and Design*, **18**: 389–401, 1995.
[14] R.K.L. Su, H.Y. Sun. Numerical Solutions of Two-Dimensional Anisotropic Crack Problems. *International Journal of Solids and Structures*, **40**: 4615-4635, 2003.
[15] J.F. Xie, S.L. Fok, A.Y.T. Leung. A Parametric Study on the Fractal Finite Element Method for Two-Dimensional Crack Problems. *International Journal for Numerical Methods in Engineering*, **58**: 631–642, 2003.
[16] R.K.L. Su, A.Y.T. Leung. Three-Dimensional Mixed Mode Analysis of a Cracked Body by Fractal Finite Element Method. *International Journal of Fracture*, **110**(1): 1–20, 2001.
[17] M.L. Williams. On the Stress Distribution at the Base of a Stationary Crack. *ASME Journal of Applied Mechanics*, **24**: 109–114, 1957.
[18] R.J. Hartranft, G.C. Sih. The Use of Eigenfunction Expansions in the General Solution of Three-Dimensional Crack Problems. *Journal of Mathematics and Mechanics*, **19**: 123–138, 1969.
[19] T. Belytschko, Y.Y. Lu, L. Gu. Element-free Galerkin Methods. *International Journal of Numerical Methods in Engineering*, **37**: 229–256, 1994.
[20] Y.Y. Lu, T. Belytschko, L. Gu. A New Implementation of the Element Free Galerkin Method. *Computer Methods in Applied Mechanics and Engineering*, **113**: 397–414, 1994.
[21] T. Belytschko, Y.Y. Lu, L. Gu. Crack Propagation by Element-Free Galerkin Methods. *Engineering Fracture Mechanics*, **51**(2): 295–315, 1995.
[22] T. Belytschko, D. Organ, Y. Krongauz. Coupled finite element-element-free Galerkin Method. *Computational Mechanics*, **17**: 186–195, 1995.
[23] Y. Krongauz, T. Belytschko. Enforcement of Essential Boundary Conditions in Meshless Approximations Using Finite Elements. *Computer Methods in Applied Mechanics and Engineering*, **131**(1–2): 133–145, 1996.
[24] P. Lancaster, K. Salkauskas. Surfaces Generated by Moving Least Squares Methods. *Mathematics of Computation*, **37**: 141–158, 1981.
[25] Y.Y. Lu, T. Belytschko, W.K. Liu. A variationally coupled FE-BE method for elasticity and fracture mechanics. *Computer Methods in Applied Mechanics and Engineering*, **85**: 21–37, 1991.
[26] B.N. Rao, S. Rahman. An Efficient Meshless Method for Fracture Analysis of Cracks. *Computational Mechanics*, **26**: 398–408, 2000.
[27] T. Belytschko, Y. Krongauz, D. Organ, M. Fleming, P. Krysl. Meshless methods: an overview and recent developments. *Computer Methods in Applied Mechanics and Engineering*, **139**: 3–47, 1996.
[28] I.V. Singh. A numerical solution of composite heat transfer problems using meshless method. *International Journal of Heat and Mass Transfer*, **47**: 2123–2138, 2004.
[29] M. Fleming, Y.A. Chu, B. Moran, T. Belytschko, Y.Y. Lu, L. Gu. Enriched Element-free Galerkin Methods for Crack-Tip Fields. *International Journal of Numerical Methods in Engineering*, **40**: 1483–1504, 1997.
[30] D.J. Organ, M. Fleming, T. Terry, T. Belytschko. Continuous Meshless Approximations for Non-Convex Bodies by Diffraction and Transparency. *Computational Mechanics*, **18**: 225–235, 1996.
[31] R. Sedgewick. *Algorithms*. Addison-Wesley, Reading, MA, 1988.
[32] F.P. Preparata, M.I. Shamos. *Computational Geometry: An Introduction*. Springer, New York, 1990.
[33] J.S. Chen, H.P. Wang. New Boundary Condition Treatments in Meshfree Computation of Contact Problems. *Computer Methods in Applied Mechanics and Engineering*, **187**(3–4): 441–468, 2000.
[34] H. Tada, P.C. Paris, G.R. Irwin. *The Stress Analysis of Cracks Handbook*. 3 edition, ASM International, 2000.
[35] T. Fett. T-Stresses in Rectangular Plates and Circular Disks. *Engineering Fracture Mechanics*, **60**(5–6): 631–652, 1998.
[36] T.L. Anderson. *Fracture Mechanics: Fundamentals and Applications*. Second Edition, CRC Press, 2005.
[37] J.P. Benthem, W.T. Koiter. *Mechanics of Fracture 1: Method of Analysis and Solutions of Crack Problems*, G.C. Sih (ed.), Noordhoff International Publishing Leyden, pp. 131–178, 1973.